

# Metastable State-Induced Consecutive Step-like Negative Differential Resistance Behaviors in Single Crystalline VO<sub>2</sub> Nanobeams

Received 00th January 20xx,  
Accepted 00th January 20xx

DOI: 10.1039/x0xx00000x

www.rsc.org/

Jung Inn Sohn,<sup>\*ab</sup> Seung Nam Cha,<sup>a</sup> Seung Bae Son,<sup>c</sup> Jong Min Kim,<sup>a</sup> Mark E. Welland,<sup>b</sup> and Woong-Ki Hong<sup>\*c</sup>

We demonstrate the current-dependent consecutive appearance of two different negative differential resistance (NDR) transitions in a single crystalline VO<sub>2</sub> nanobeam epitaxially grown on a c-cut sapphire substrate. It is revealed that the first NDR occurs at an approximately constant current level as a result of the carrier injection-induced transition, independent of a thermally induced phase transition. In contrast, it is observed that the second NDR exhibits a temperature-dependent behavior and current values triggering the metal-insulator transition (MIT) are strongly mediated by Joule heating effects in a phase coexisting temperature range. Moreover, we find that the electrically and thermally triggered MIT behavior can be closely related with the alternate occurrence of current-induced multiple insulating and metallic phase coexistence in the nanobeam. These findings afford that the current density passing through VO<sub>2</sub> plays a critical role in both the electrical and structural phase transitions.

## Introduction

Vanadium dioxide (VO<sub>2</sub>) is a typical strongly correlated transition metal oxide that undergoes a first-order metal-insulator transition (MIT) coupled with a reversible crystal-to-crystal structural phase transition from a high-temperature tetragonal rutile (R)-type phase to a low-temperature monoclinic (M) phase at a temperature of approximately 340 K.<sup>1-2</sup> Across this crossover transition point, remarkable changes in the electrical and optical properties of VO<sub>2</sub> manifest in a dramatic amplification of the charge carrier density, offering potential applications such as threshold switching devices,<sup>3</sup> sensors,<sup>4-5</sup> memory devices,<sup>6-7</sup> and oscillators.<sup>8</sup> However, it has been a topic of controversy for decades as to whether the driving force behind the MIT is an electron-correlation-driven Mott transition or a structure-distortion-driven Peierls transition. A cooperative mechanism in the phase transformation process, such as either a Mott-assisted Peierls transition or a Peierls-assisted Mott transition, has also been proposed as an alternative to the two abovementioned driving mechanisms of the MIT because both the structural and

electron-correlation aspects are important for describing the MIT behavior in VO<sub>2</sub>.<sup>9-12</sup> Accordingly, in recent years, one-dimensional single crystalline VO<sub>2</sub> structures have been intensively investigated to comprehensively understand the nature of MIT because metallic and insulating phase domain configurations can be one-dimensionally aligned and significantly altered through the manipulation of external stimuli (thermal, mechanical, and optical as well as electrical).<sup>13-15</sup> It has been well established that the electronic phase transformation is accompanied by a crystal structure change from the metallic rutile lattice to the insulating monoclinic lattice structure widely known as the M1 phase, which is the most stable insulating phase for undoped and strain-free VO<sub>2</sub> at room temperature. Recently, however, it has been reported that during the MIT of the insulating M1 to metallic R phase, another insulating monoclinic phase, M2, can be organized and stabilized by either doping or strain.<sup>4,16-25</sup> Importantly, the M2 phase is regarded as an intermediate state between the M1 and R phases, and its resistivity is three times higher than that of the M1 phase.<sup>15,18,20</sup> These electronic and structural features of the M2 phase have a profound influence on the electrical properties and dynamic behavior of structural phase transitions.<sup>4,16-25</sup> In particular, the physical nature of inhomogeneity or multiple phase coexistence and spatial domain wall variations in the first order MIT of VO<sub>2</sub> play a crucial role in understanding the underlying physical driving mechanism for the MIT and the exact interplay of the concomitant changes in the electronic and structural phase transition properties when the intermediate M2 phase is involved.

<sup>a</sup> Department of Engineering Science, University of Oxford, Oxford OX1 3PJ, United Kingdom

<sup>b</sup> Nanoscience Centre, University of Cambridge, Cambridge CB3 0FF, United Kingdom

<sup>c</sup> Jeonju Center, Korea Basic Science Institute, Jeonju, Jeollabuk-do 54907, Republic of Korea

E-mail: junginn.sohn@eng.ox.ac.uk; wkh27@kbsi.re.kr

Electronic Supplementary Information (ESI) available: See DOI: 10.1039/x0xx00000x

Here, we present the observation of an intermediate-state induced step-like negative differential resistance (NDR) behavior in current-controlled two-terminal VO<sub>2</sub> nanobeam devices. The two-terminal devices were fabricated using VO<sub>2</sub> nanobeams that were epitaxially grown on a c-cut sapphire to employ the fundamental principle of adhesive interactions between the VO<sub>2</sub> nanobeam and the substrate. The strain energy associated with interfacial adhesion interactions is the major driving force for self-organized metal-insulator domains and multiple insulating phases along the nanobeam axis, which can play a critical role in the motion of domains and the heat conduction by Peltier and Joule heating effects upon the current flow through the nanobeam.<sup>25,26</sup> Intriguingly, current-dependent consecutive step-like NDR regions with two distinctly different transition behavior properties were observed in the current-voltage (I-V) characteristics of the epitaxial VO<sub>2</sub> nanobeam device around the coexisting temperature range of metal-insulator phases. This result is closely related with the alternate occurrence of current-induced metastable states in the nanobeams as a path for carrying an electric current.

## Results and discussion

Transmission electron microscope (TEM) examinations were carried out to characterize the growth direction and crystal structure of the VO<sub>2</sub> nanobeams that were epitaxially grown on a c-cut sapphire substrate, as shown in Figure 1. Figure 1(a) shows a typical optical microscopy image for the epitaxial VO<sub>2</sub> nanobeams grown laterally along three equivalent  $\langle 11\bar{2}0 \rangle$  directions on the c-plane sapphire surface. The angles between the VO<sub>2</sub> nanobeams were 60°, 120°, or parallel to each other. Figure 1(b) shows low magnification

TEM images from the cross-section of the interface between the VO<sub>2</sub> nanobeam and the sapphire substrate. Figures 1(c) and 1(d) show high-resolution (HR) TEM images and the corresponding selected area electron diffraction (SAED) patterns (the insets) taken from the VO<sub>2</sub> nanobeam (marked as ① in Figure 1(b)) and the sapphire substrate (marked as ② in Figure 1(b)), respectively. In Figure 1(c), the marked lattice spacings of 0.459 and 0.484 nm correspond to the inter-plane spacing of the (010) and (001) planes of the monoclinic VO<sub>2</sub> nanobeam, respectively. Furthermore, the SAED patterns indexed to the monoclinic VO<sub>2</sub> structure confirm that the crystalline orientation relationship between the VO<sub>2</sub> nanobeam and the c-cut sapphire is (010) VO<sub>2</sub>//(0001) sapphire, which is consistent with previously reported results.<sup>27</sup> These results reveal that the VO<sub>2</sub> nanobeam with a triangular cross section has (01 $\bar{1}$ ) and (011) side facets and a (010) bottom surface.

Figure 2(a) shows the electrical resistance as a function of temperature upon heating and cooling in the two-terminal device made directly from the VO<sub>2</sub> nanobeam epitaxially grown on the c-cut sapphire substrate (the inset of Figure 2(a)). The length and the width of the nanobeams used in the electrical experiments were found to be between 3 and 5  $\mu\text{m}$  and between 150 and 250 nm, respectively. The resistance varied gradually with temperature upon heating and cooling, and then, an abrupt change in resistance occurred at the critical temperature (marked by a grey-colored region in the left panel of Figure 2(a)) wherein the accompanying phase transition can induce a significant change in the free carrier density. As shown in the right panel of Figure 2(a), it is known that the MIT is induced by the symmetric splitting of the t<sub>2g</sub> band composed of 3d vanadium states, accompanied by a crystallographic transformation from the M to R phase.<sup>25,28,29</sup>

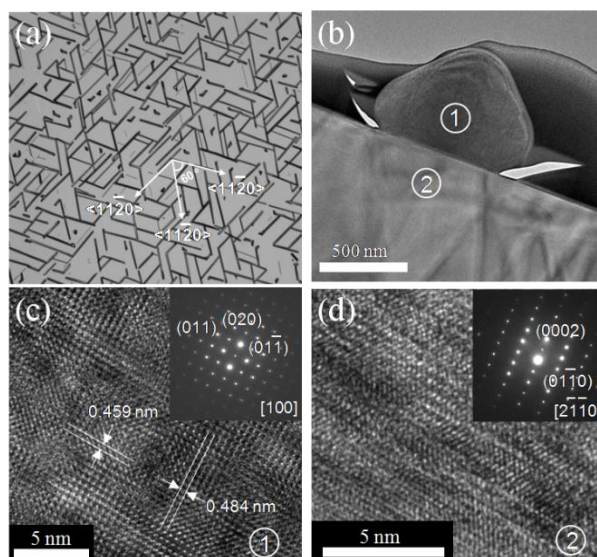


**Figure 1.** (a) Structural characterization of single crystalline VO<sub>2</sub> nanobeams grown on a c-plane sapphire substrate. (a) An optical microscopy image of VO<sub>2</sub> nanobeams grown laterally along three equivalent directions on the c-plane sapphire. (b) A low magnification TEM image and (c) high resolution TEM images obtained from the cross-section of the interface between a single VO<sub>2</sub> nanobeam and a sapphire substrate. The insets in (c) and (d) show the corresponding SAED patterns on the monoclinic VO<sub>2</sub> nanobeam (marked as ①) and the sapphire (marked as ②) taken at [100] and [21 $\bar{1}$ 0] zone axes, respectively.

In Figure 2(a), the resistance of the VO<sub>2</sub> nanobeam initially follows a thermally activated behavior with an activation energy ( $E_a$ ) of approximately 0.21 eV in the insulating phase regime, and the transition temperature is shifted upwards during both heating and cooling due to the strain effects on the appearance of the coexisting phase region in the vicinity of the MITs, which is consistent with previously reported results.<sup>30–33</sup> Figure 2(b) shows I-V characteristics for the epitaxial VO<sub>2</sub> nanobeam device with a lower threshold current ( $I_{th,low}$ ) (marked by a blue-colored region) and upper threshold current ( $I_{th,up}$ ) (marked by a red-colored region) at threshold switching voltages ( $V_{th}$ ) during cooling from 70 to 30 °C. It can be seen that the  $V_{th}$  and the  $I_{th,up}$  considerably decreased with increasing temperature, which is attributed to the resistance switching to the metallic state. Interestingly, however, the  $I_{th,low}$  was found to have very similar values with small variations regardless of the temperature, as shown in Figure 2(c), which is in good agreement with the results of our simulations in Figure 3.

In order to assess how much Joule heating can thermally induce a temperature rise and affect a phase transition behaviour, here, we calculated the temperature increase in the device as a function of varying thermal environments ranging from 40 to 70 °C using COMSOL Multiphysics. We modelled the thermal phenomena in the VO<sub>2</sub> nanobeam device by considering two primary heat generation and dissipation processes involving heat conduction loss through the substrate from the VO<sub>2</sub> bottom surface and convective

heat transfer to the ambient from the remaining surfaces of the nanobeam. Note that we neglected radiative heat loss because the radiation heat transfer to the surroundings can be estimated to be exceedingly low for our device system where the maximum temperature rise is below 100 °C. Based on these basic models for heat transfer kinetics, we assumed that the VO<sub>2</sub> nanobeam bottom surface was thermally anchored to the device (substrate) temperature and the other surfaces were anchored to the ambient. Then, simulation parameters, such as thermal conductivity (690 Jkg<sup>-1</sup>K<sup>-1</sup>), specific heat, mass density (4340 kgm<sup>-3</sup>), and heat transfer (10 Wm<sup>-2</sup>K<sup>-1</sup>), were taken from literatures (Table S1 in the Supplementary Information).<sup>34–37</sup> Figure 3 shows numerical simulation results, exhibiting a small steady-state temperature increase in the device temperature range between 40 and 70 °C. The simulated temperature under conditions of the  $V_{th}$  and the  $I_{th,low}$ , which were extracted from the blue-colored regions in Figure 2(b), was found to increase from approximately 2.6 to 4.6 °C while increasing the measurement device temperature from 40 to 70 °C. This result is consistent with the result reported by Zimmers *et al.*<sup>38</sup> in which the heating was modelled using  $T_{model} = T_{set} + \alpha IV$  for the two-terminal VO<sub>2</sub> film device with the gap length of 10 and 20 μm. They showed the thermally induced insulator-metal transition due to the local temperature rise at only higher DC voltages (> 15 V) and not at low voltages (< 10 V). In our work, the maximum temperature rise was estimated to be approximately less than 5 °C, which is below the transition temperature of the VO<sub>2</sub> nanobeam shown in Figure 2(a) (also see

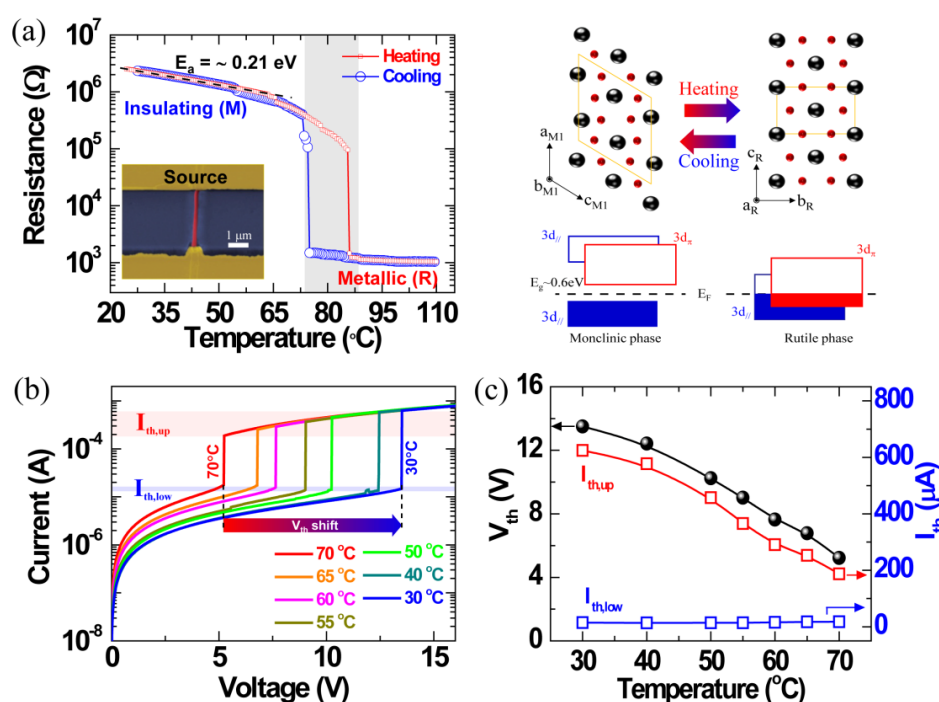


**Figure 2.** Changes in the resistance, crystal structure, and electrical properties of a VO<sub>2</sub> nanobeam. (a) Resistance change of the VO<sub>2</sub> nanobeam during heating and cooling cycles. The inset shows an SEM image of a representative two-terminal device made directly from the VO<sub>2</sub> nanobeam grown on the c-plane sapphire substrate. The right panel shows crystal structure change of the VO<sub>2</sub> nanobeam during heating and cooling cycles. (b) Current-voltage characteristics for the two terminal device of the nanobeam with threshold switching voltages during cooling. The blue-colored and red-colored regions show the lower and upper threshold current at the threshold switching voltages during cooling from 70 to 30 °C. (c) Changes in threshold switching voltages and threshold currents obtained from (b).

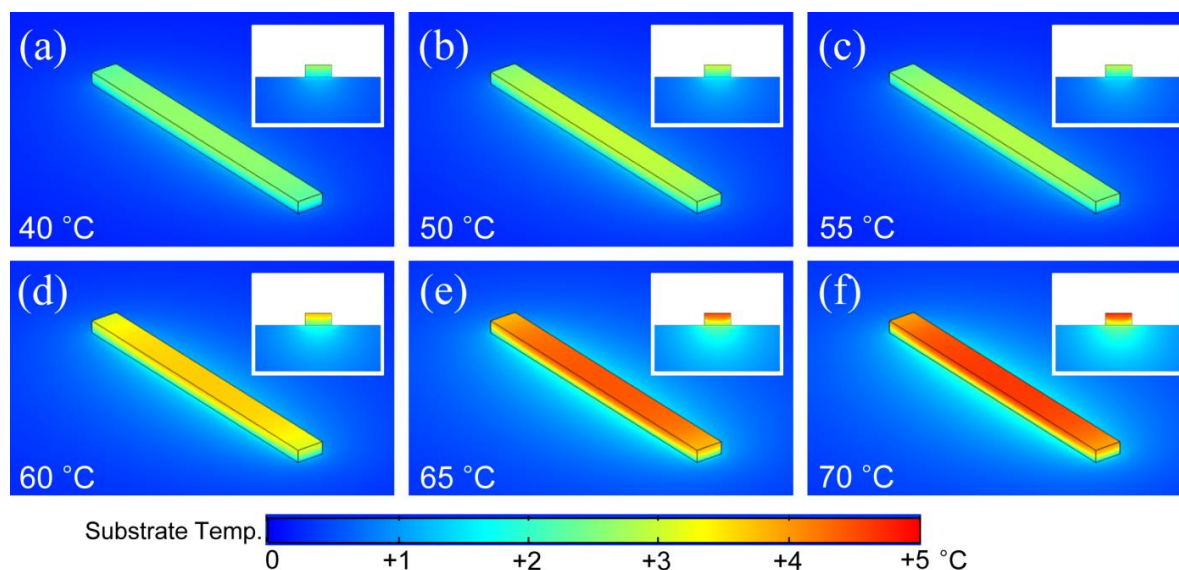


**Figure 3.** Simulated temperature rise at different device temperatures showing Joule heating effects on the c-cut sapphire substrate.

Table S2 and Figures S1-S3 in the Supplementary Information). These simulation results indicate that the Joule heating is insufficient to trigger a thermally induced phase transition by itself. Thus, we speculate that the phase transition in the epitaxial VO<sub>2</sub> nanobeam device might be initially triggered at a certain critical current density, independent of the device temperature associated with the Joule heating around the coexisting temperature range of metal-insulator phases.

In recent studies, an electronically induced insulator-metal phase transition was investigated in the lateral and vertical junction devices made from a VO<sub>2</sub> film.<sup>39,40</sup> Yang *et al.*<sup>39</sup> suggested that non-thermal mechanisms rather than only Joule heating effects may contribute to the phase transition from 77 K to 300 K based on the temperature dependence of the transition voltage and the hysteresis width. They also showed that carrier injection under applied bias may play a critical role in the phase transition of VO<sub>2</sub>. Joushaghani *et al.*<sup>40</sup> demonstrated the combined effects of carrier injection and thermal redistribution in the insulator-metal phase transition in VO<sub>2</sub> nano-gap junctions based on applied voltages on a time scale and the length of nano-gap. To further probe the electrical evolution of the epitaxial VO<sub>2</sub> nanobeams, the detailed switching behavior was investigated with the same VO<sub>2</sub>-based two-terminal device shown in Figure 2 in the vicinity of the phase transition temperature, whereby multiple insulating and metallic phases and their coexistence phases are available. Figures 4(b) and (d) show the I-V characteristics of the epitaxial VO<sub>2</sub> nanobeam device with variable external load resistors ( $R_{\text{ext}}$ ) in series (Figure 4(a)) at 65 °C for a voltage-sweeping mode (V-mode). Figures 4(b) and (c) show I-V behavior characteristics acquired while sweeping the voltage up and down (marked by arrows) and obtained with a series resistance of 10 and 51 k $\Omega$ , respectively, to control the amount of the maximum (upper) currents flowing through the VO<sub>2</sub> nanobeam (also see Figure S4 in the Supplementary

Information for a series resistance of 100 k $\Omega$ ). We observed that the I-V curves show two threshold voltages of  $V_{\text{th}\uparrow}$  (forward) and  $V_{\text{th}\downarrow}$  (backward) (marked by black circles), resulting in hysteresis. Initially, the current increased smoothly with increasing the voltage and then the current abruptly jumped by orders of magnitude at  $V_{\text{th}\uparrow}$ , switching to a highly conducting state. When the bias voltage was lowered from the high conducting state, the device returned to the insulating state at  $V_{\text{th}\downarrow}$ . Explicitly, it was observed that for  $R_{\text{ext}} = 10$  k $\Omega$ , the VO<sub>2</sub> nanobeam device exhibited a large hysteresis width, whereas for the case of  $R_{\text{ext}} = 51$  k $\Omega$ , the hysteresis width was significantly reduced and became almost negligible (also see Figure S4 in the Supplementary Information). Interestingly, it is clearly seen that the forward threshold voltages ( $V_{\text{th}\uparrow}$ ) and lower threshold currents ( $I_{\text{th,low}}$ ) were unchanged for the epitaxial VO<sub>2</sub> nanobeam regardless of the resistance values of the series resistors, when the voltage was swept from 0 to 7 V (forward), whereas the backward threshold voltage ( $V_{\text{th}\downarrow}$ ) of the same device with the lower series resistance was significantly shifted towards lower values, leading to the large hysteresis, when the voltage sweep was reversed from 7 to 0 V (backward). Here, it should be noted that the device with the larger series resistance exhibits a low  $I_{\text{th,up}}$  level as the current passing through the VO<sub>2</sub> nanobeam was considerably reduced after the transition through the voltage drop in the series resistor. This indicates that the large hysteresis is probably associated with thermal heating effects induced by current density through the epitaxial VO<sub>2</sub> nanobeam. These findings have profound implications for the critical role of the current density on both the electrical and structural phase transitions. To further clarify whether the forward threshold voltage associated with the abrupt resistive switching behavior in our VO<sub>2</sub> nanobeam device depends on the voltage switching time, affecting the occurrence of Joule heating, we carried out I-V measurements at 65 °C by applying either DC bias or pulsed



voltages, as shown in Figure 4(d) (also see Figure S5 in the Supplementary Information). The pulsed I-V curve shows an abrupt transition at approximately the same critical voltage as that of the DC measurement, indicating that the  $V_{th\uparrow}$  was not significantly affected by bias conditions or the pulse width, resulting in Joule heating. These results suggest that the current control flowing through  $VO_2$  is more important and significantly attributed not only to the initial triggering of the MITs but also to the development of a hysteretic phase transition behavior associated with the first-order phase transformation character after the large increase in conductivity from the transition.

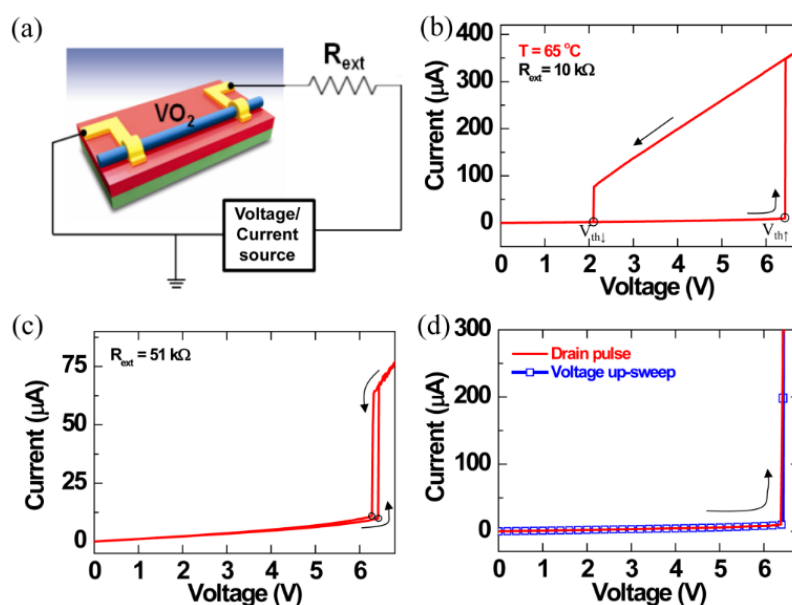
Recently, Favaloro *et al.*<sup>25</sup> directly observed highly localized alternating Peltier and Joule effects at the metal-insulator domain walls of  $VO_2$  nanobeams under current bias in the metal-insulator coexisting phase regime. They limited the bias current amplitudes to approximately 15  $\mu A$  so that the  $VO_2$  nanobeam was not displaced by electrothermal effects in the metal-insulator coexisting state.<sup>25</sup> Unlike a previous study,<sup>25</sup> in order to precisely address and understand the role of the current density during MITs in this work, the I-V characteristics of the  $VO_2$  nanobeam device were investigated with a current-sweeping mode (I-mode) at different temperatures, as shown in Figures 5 and S6. Figure 5(a) shows an I-V curve obtained in an I-mode at  $T = 65^\circ C$  for the same  $VO_2$  nanobeam device as shown in Figures 2 and 3. Intriguingly, two distinct consecutive NDR phenomena (steps II and IV in Figure 5(a)) were observed. It was clearly revealed that the first NDR (step II) occurs at an approximately constant certain current level independent of temperature (also see Figure S6 in the Supplementary Information). Note that the current value inducing the first NDR is quite similar to the lower threshold current shown in

Figure 2. Thus, it is believed that the first NDR is a result of the carrier injection-induced transition around the coexisting temperature range of metal-insulator phases independent of a thermally induced transition (Joule heating effect).<sup>41,42</sup> In contrast, it was observed that the second NDR (step IV) behavior occurs differently, and the current values triggering the MIT strongly depend on the device temperature. While increasing the temperature of the epitaxial  $VO_2$  nanobeam device, the phase transition is more stimulated thermally, hence further leading to towards the metallic state. Moreover, in such a high current regime after the first MIT, the MIT can be sufficiently triggered by Joule heating effects associated with the excess current flowing through the device. Therefore, we suggest that as the temperature increases, the second NDR phenomenon is observed at a relatively lower current level ( $I_{th,up}$ ) (Figure S6), indicating the different trigger mechanism for the phase transition compared to the first NDR. Thermal effects due to the Joule heating can also be considered as a prime driving force for the continuous conversion from the insulating to metallic phases with the current at step III and play a critical role in the full transformation into the metallic phase (step V).

To further understand the contribution of the charge carrier injection to the consecutive step-like NDR phenomena, threshold resistivity ( $\rho_{th}$ ) values were estimated at the transition points of different temperatures (step I), enabling to the identification of multiple phases and relative amounts of phases formed within the epitaxial  $VO_2$  nanobeam. The  $\rho_{th}$  can be extracted from the following equation,<sup>18,25,43</sup>

$$R_{tot} = x\rho_{i,c}L/A + (1-x)\rho_{m,c}L/A + R_c + R_{dw} \quad (1)$$

where  $R_{tot}$  is the total resistance,  $x$  is the fraction of insulating states in the  $VO_2$  nanobeam,  $L$  is the length between the



**Figure 4.** Current-voltage (I-V) characteristics for a  $VO_2$  nanobeam grown on the c-plane sapphire substrate. (a) A schematic diagram of the  $VO_2$  nanobeam device connected in series with an external load resistance ( $R_{ext}$ ). Representative current-voltage characteristics measured consecutively at  $65^\circ C$  by varying the applied voltage both in the forward- and reverse-sweep from 0 to 7 V for the  $VO_2$  nanobeam device with an external resistor of (b) 10 k $\Omega$  and (c) 51 k $\Omega$ . (d) I-V characteristics of the  $VO_2$  nanobeam device with  $R_{ext} = 10$  k $\Omega$  measured after the application of pulse voltage.

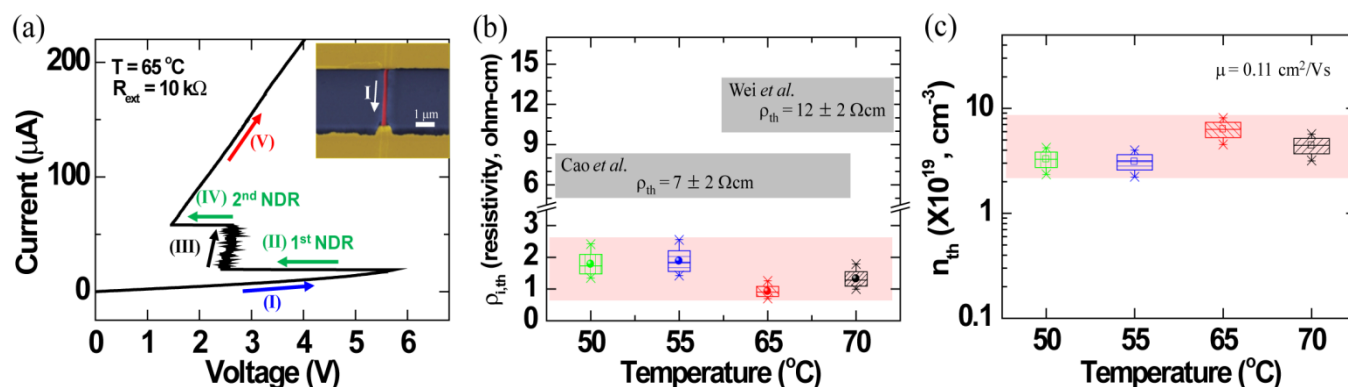


**Figure 5.** (a) Current-voltage characteristics of the VO<sub>2</sub> nanobeam device with  $R_{\text{ext}} = 10 \text{ k}\Omega$  measured for the current-controlled mode (steps I)-(V)) in the VO<sub>2</sub> nanobeam with coexisting phases. (b) Threshold resistivity and (c) threshold carrier concentration (assuming a carrier mobility of  $0.11 \text{ cm}^2/\text{Vs}$ ) at the transition point (step I  $\rightarrow$  II) as a function of temperature for the current-mode measurement.

source and drain electrodes,  $A$  is the cross-sectional area of the nanobeam,  $\rho_{i,c}$  and  $\rho_{m,c}$  are the resistivity values of the insulating and metallic phases in the coexisting phase regime, respectively,  $R_c$  is the contact resistance, and  $R_{dw}$  is the resistance of a domain wall. From equation (1), in the case of the predominant insulating domains (step I),  $R_{\text{tot}} \approx x\rho_{i,c}L/A$  in which  $I_{\text{th,low}}$  is independent of temperature.  $R_c$  and  $R_{dw}$  are negligible since they are much lower resistance compared to the insulating state of VO<sub>2</sub>.<sup>18,43,45</sup> This can be related to the first NDR region. In the case that metallic domains are dominant,

$R_{\text{tot}} \approx x\rho_{i,c}L/A + (1-x)\rho_{m,c}L/A + R_{dw}$ , which is related to the second NDR region due to the temperature dependence. When  $x$  is in a range between 0.5 and 1, the constant threshold resistivity ( $\rho_{\text{th}}$ ) at the transition point (I $\rightarrow$ II) was found to be in the range between 0.7–2.6 ohm-cm, as shown in Figure 5(b). Similar behavior for the MIT has also been reported for VO<sub>2</sub> microcrystals by Wei *et al.*<sup>18</sup> and Cao *et al.*<sup>45</sup> (Figure 5(b)). Assuming a carrier mobility of  $\mu = 0.11 \text{ cm}^2\text{V}^{-1}\text{s}^{-1}$  reported for VO<sub>2</sub> thin films,<sup>43,44</sup> we can estimate a threshold carrier density ( $n_{\text{th}}$ ) in our epitaxial VO<sub>2</sub> nanobeam to be in the range between  $8.1 \times 10^{19}$  and  $2.2 \times 10^{19} \text{ cm}^{-3}$  (Figure 5(c)), which is comparable with previous reports.<sup>34,46</sup> However, during the step I, the epitaxial VO<sub>2</sub> nanobeam is in a highly resistive state in the coexisting insulator and metal phases present at the transition point. The progressive increase of the current density beyond the critical threshold carrier density can result in a gradual increase in the metallic phase fraction,<sup>19,47</sup> leading to the nucleation and stabilization of the M2 phase due to an axial tensile stress at the insulator/metal phase boundaries (also see Figure S7 in the Supplementary Information).<sup>18,20,47</sup> It is known that the resistivity of the M2 phase is 3 times higher than that of the M1 phase.<sup>15,18,20</sup> Therefore, it is suggested that the step III region is responsible for the continuous conversion and growth toward metallic R phases as well as nucleation of the M2 phases.

## Conclusions

In summary, we have presented the observation of an intermediate-state induced step-like NDR behavior in a single crystalline VO<sub>2</sub> nanobeam epitaxially grown on a c-cut sapphire

substrate. The two-terminal devices were fabricated using epitaxial VO<sub>2</sub> nanobeams to employ adhesive interactions between the VO<sub>2</sub> nanobeam and the substrate, which can induce self-organized metal-insulator domains and multiple insulating monoclinic phases along the nanobeam axis. Intriguingly, current-dependent consecutive step-like NDR regions with two distinctly different transition behavior properties were observed in the current-voltage (I-V) characteristics of the epitaxial VO<sub>2</sub> nanobeam device around the metal-insulator phase coexisting temperature range. It was revealed that the first NDR occurred at an approximately constant current level as a result of the carrier injection-induced transition, independent of a thermally induced phase transition. In contrast, the second NDR exhibited a temperature-dependent behavior, and the current values triggering the metal-insulator transition were strongly mediated by Joule heating effects in the phase coexisting temperature range. This result is closely related to the alternate occurrence of current-induced metastable states in the nanobeams as a path for carrying an electric current. Our study shows that the current density passing through a single crystalline VO<sub>2</sub> nanobeam plays a critical role in both the electrical and structural phase transitions.

## Experimental section

All of the VO<sub>2</sub> nanobeams used in this work were grown on c-cut sapphire substrates by a vapor phase transport process, as described elsewhere.<sup>27</sup> The VO<sub>2</sub> nanobeams were single-crystalline with a monoclinic structure (Figure 1). For structural analysis, we used an FEI transmission electron microscope (TEM, Tecnai) operated at 300 KeV. To investigate the electrically probing of the MIT in VO<sub>2</sub> nanobeams, the two-terminal devices were fabricated using VO<sub>2</sub> nanobeams that were grown epitaxially on a c-cut sapphire substrate. For the epitaxial VO<sub>2</sub> nanobeam devices, metal electrodes consisting of Ti (80 nm thick)/Au (100 nm thick) were deposited by an electron beam evaporator, and they were defined as source and drain electrodes by photolithography followed by lift-off processes. The distance between the source and drain

electrodes is approximately 3  $\mu\text{m}$ , as shown in the inset of Figures 2a and 4a. Here, metal electrodes were directly deposited on the epitaxial  $\text{VO}_2$  nanobeams grown on the c-cut sapphire. The electrical properties of the  $\text{VO}_2$  nanobeam devices were measured in air using a semiconductor characterization system (Keithley 4200-SCS).

## Acknowledgements

W.-K.H acknowledges the financial support from KBSI grant (T36417) and the National Research Foundation of Korea (NRF) grant funded by the Korean Government (NRF-2013-R1A1A2009884). J.I.S and M.E.W acknowledge the financial support from the European Community's Seventh Framework Programme (FP7/2007-2013) under grant agreement No. 216777, Project "Nanocomputing Building blocks with Acquired Behaviour (NABAB)".

## Notes and references

- 1 F. J. Morin, *Phys. Rev. Lett.* 1959, **3**, 34.
- 2 M. Nakano, K. Shibuya, D. Okuyama, T. Hatano, S. Ono, M. Kawasaki, Y. Iwasa, Y. Tokura, *Nature* 2012, **487**, 459.
- 3 N. Shukla, A. V. Thathachary, A. Agrawal, H. Paik, A. Aziz, D. G. Schlom, S. K. Gupta, R. Engel-Herbert, S. Datta, *Nat. Commun.* 2015, **6**, 7812.
- 4 B. Hu, Y. Ding, W. Chen, D. Kulkarni, Y. Shen, V. V. Tsukruk, Z. L. Wang, *Adv. Mater.* 2010, **22**, 5134.
- 5 E. Strelcov, Y. Lilach, A. Kolmakov, *Nano Lett.* 2009, **9**, 2322.
- 6 R. Xie, C. T. Bui, B. Varghese, Q. Zhang, C. H. Sow, B. Li, J. T. L. Thong, *Adv. Funct. Mater.*, 2011, **21**, 1602.
- 7 S. H. Bae, S. Lee, H. Koo, L. Lin, B. H. Jo, C. Park, Z. L. Wang, *Adv. Mater.* 2013, **25**, 5098.
- 8 N. Shukla, A. Parihar, E. Freeman, H. Paik, G. Stone, V. Narayanan, H. Wen, Z. Cai, V. Gopalan, R. Engel-Herbert, D. G. Schlom, A. Raychowdhury, S. Datta, *Sci. Rep.* 2014, **5**, 4964.
- 9 M. W. Haverkort, Z. Hu, A. Tanaka, W. Reichelt, S. V. Streltsov, M. A. Korotin, V. I. Anisimov, H. H. Hsieh, H. -J. Lin, C. T. Chen, D. I. Khomskii, L. H. Tjeng, *Phys. Rev. Lett.* 2005, **95**, 196404.
- 10 S. Biermann, A. Poteryaev, A. I. Lichtenstein, A. Georges, *Phys. Rev. Lett.* 2005, **94**, 026404.
- 11 T. C. Koethe, Z. Hu, M. W. Haverkort, C. Schüßler-Langeheine, F. Venturini, N. B. Brookes, O. Tjernberg, W. Reichelt, H. H. Hsieh, H. -J. Lin, C. T. Chen, L. H. Tjeng, *Phys. Rev. Lett.* 2006, **97**, 116402.
- 12 T. Yao, X. Zhang, Z. Sun, S. Liu, Y. Huang, Y. Xie, C. Wu, X. Yuan, W. Zhang, Z. Wu, G. Pan, F. Hu, L. Wu, Q. Liu, S. Wei, *Phys. Rev. Lett.* 2010, **105**, 226405.
- 13 J. Cao, E. Ertekin, V. Srinivasan, W. Fan, S. Huang, H. Zheng, J. W. L. Yim, D. R. Khanal, D. F. Ogletree, J. C. Grossman, J. Wu, *Nat. Nanotechnol.* 2009, **4**, 732.
- 14 T. S. Kasirga, D. Sun, J. H. Park, J. M. Coy, Z. Fei, X. Xu, D. H. Cobden, *Nat. Nanotechnol.* 2012, **7**, 723.
- 15 J. H. Park, J. M. Coy, T. S. Kasirga, C. Huang, Z. Fei, S. Hunter, D. H. Cobden, *Nature* 2013, **500**, 431.
- 16 J. I. Sohn, H. J. Joo, D. Ahn, H. H. Lee, A. E. Porter, K. Kim, D. J. Kang, M. E. Welland, *Nano Lett.* 2009, **9**, 3392.
- 17 J. I. Sohn, H. J. Joo, K. S. Kim, H. W. Yang, A. -R. Jang, D. Ahn, H. H. Lee, S. N. Cha, D. J. Kang, J. M. Kim, *Nanotechnology* 2012, **23**, 205707.
- 18 J. Wei, Z. Wang, W. Chen, D. H. Cobden, *Nat. Nanotechnol.* 2009, **4**, 420.
- 19 S. Zhang, J. Y. Chou, L. J. Lauhon, *Nano Lett.* 2009, **9**, 4527.
- 20 J. Cao, Y. Gu, W. Fan, L. Q. Chen, D. F. Ogletree, K. Chen, N. Tamura, M. Kunz, C. Barrett, J. Seidel, J. Wu, *Nano Lett.* 2010, **10**, 2667.
- 21 A. Tselev, J. D. Budai, E. Strelcov, J. Z. Tischler, A. Kolmakov, S. V. Kalinin, *Nano Lett.* 2011, **11**, 3065.
- 22 H. Guo, K. Chen, Y. Oh, K. Wang, C. Dejoie, S. A. S. Asif, O. L. Warren, Z. W. Shan, J. Wu, A. M. Minor, *Nano Lett.* 2011, **11**, 3207.
- 23 E. Strelcov, A. Tselev, I. Ivanov, J. D. Budai, J. Zhang, J. Z. Tischler, I. Kravchenko, S. V. Kalinin, A. Kolmakov, *Nano Lett.* 2012, **12**, 6198.
- 24 J. M. Atkin, S. Berweger, E. K. Chavez, M. B. Raschke, J. Cao, W. Fan, J. Wu, *Phys. Rev. B* 2012, **85**, 020101(R).
- 25 T. Favaloro, J. Suh, B. Vermeersch, K. Liu, Y. Gu, L. -Q. Chen, K. X. Wang, J. Wu, *Nano Lett.* 2014, **14**, 2394.
- 26 Q. Gu, A. Falk, J. Wu, L. Ouyang, H. Park, *Nano Lett.* 2007, **7**, 363.
- 27 J. I. Sohn, H. J. Joo, A. E. Porter, C. -J. Choi, K. Kim, D. J. Kang, M. E. Welland, *Nano Lett.* 2007, **7**, 1570.
- 28 V. Ann. Eyert, *Ann. Phys. Berlin* 2002, **11**, 650.
- 29 Y. Wu, L. Fan, W. Huang, S. Chen, S. Chen, F. Chen, C. Zou, Z. Wu, *Phys. Chem. Chem. Phys.* 2014, **16**, 17705.
- 30 H. W. Verleur, Jr. A. S. Barker, C. N. Berglund, *Phys. Rev.* 1968, **172**, 788.
- 31 W. H. Rosevear, W. Paul, *Phys. Rev. B* 1973, **7**, 2109.
- 32 A. Beaumont, J. Leroy, J. -C. Orlianges, A. Crunteanu, *J. Appl. Phys.* 2014, **115**, 154502.
- 33 W. Fan, J. Cao, J. Seidel, Y. Gu, J. W. Yim, C. Barrett, K. M. Yu, J. Ji, R. Ramesh, L. Q. Chen, J. Wu, *Phys. Rev. B* 2011, **83**, 235102.
- 34 G. Stefanovich, A. Pergament, D. Stefanovich, *J. Phys.: Condens. Matter.* 2000, **12**, 8837.
- 35 G. Gopalakrishnan, D. Ruzmetov, S. Ramanathan, *J. Mater. Sci.* 2009, **44**, 5345.
- 36 C. N. Berglund, H. J. Guggenheim, *Phys. Rev.* 1969, **185**, 1022.
- 37 Z. Yan, G. Liu, J. M. Khan, A. A. Balandin, *Nat. Commun.* 2012, **3**, 827.
- 38 A. Zimmers, L. Aigouy, M. Mortier, A. Sharoni, S. Wang, *Phys. Rev. Lett.* 2013, **110**, 056601.
- 39 Z. Yang, S. Hart, C. Ko, A. Yacoby, S. Ramanathan, *J. Appl. Phys.* 2011, **110**, 033725.
- 40 A. Joushaghani, J. Jeong, S. Paradis, D. Alain, J. S. Aitchison, J. K. S. Poon, *Appl. Phys. Lett.* 2014, **104**, 221904.
- 41 F. H. Chen, L. L. Fan, S. Chen, G. M. Liao, Y. L. Chen, P. Wu, L. Song, C. W. Zou, Z. Y. Wu, *ACS Appl. Mater. Interfaces* 2015, **7**, 6875.
- 42 S. Zhang, M. A. Kats, Y. Cui, Y. Zhou, Y. Yao, S. Ramanathan, F. Capasso, *Appl. Phys. Lett.* 2014, **105**, 211104.
- 43 J. Cao, W. Fan, H. Zheng, J. Wu, *Nano Lett.* 2009, **9**, 4001.
- 44 D. Ruzmetov, D. Heiman, B. B. Clafflin, V. Narayanamurti, S. Ramanathan, *Phys. Rev. B* 2009, **79**, 153107.
- 45 J. Cao, W. Fan, K. Chen, N. Tamura, M. Kunz, V. Eyert, J. Wu, *Phys. Rev. B* 2010, **82**, 241101(R).
- 46 A. Pergament, *J. Phys.: Condens. Matter.* 2003, **15**, 3217.
- 47 A. Tselev, I. A. Luk'yanchuk, I. N. Ivanov, J. D. Budai, J. Z. Tischler, E. Strelcov, A. Kolmakov, S. V. Kalinin, *Nano Lett.* 2010, **10**, 4409.